

2D AND 3D TRAJECTORY PLANNING FOR UAVS FORMATION SYSTEM USING DYNAMIC WINDOW APPROACH

Rongbo Zhu[1], Kai You[1], Huicheng Yang[1], Xukang Ma[1] & Zhenli Chen[1,2]

[1]School of Aeronautics, Northwestern Polytechnical University, Xi'an 710072, China
[2]National Key Laboratory of Aircraft Configuration Design, Xi'an 710072, China

Abstract

Formation flight can effectively reduce the drag of wingmen, thereby lowering fuel consumption and extending the flight range. For unmanned aerial vehicle (UAV) formations, however, these benefits must be achieved while satisfying obstacle-avoidance and flight-performance constraints. Since the relative formation position affects both the lift-to-drag ratio and the positional stability derivatives, trajectory planning and formation shape optimization should be considered together. This paper studies two-dimensional and three-dimensional trajectory planning for a UAV formation using a leader-first strategy. The trajectory of the lead aircraft is planned by the dynamic window approach (DWA), and the wingmen's trajectories are then generated according to the prescribed formation geometry. In the three-dimensional case, climb angle and velocity constraints are introduced into the planning process, and formation contraction, rotation, transformation, and recovery are used to support obstacle avoidance. For the cruise phase, a formation shape optimization model is further established based on the SACCON configuration. The vortex lattice method (VLM) is used to evaluate the aerodynamic performance and stability derivatives, and NSGA-II is employed to obtain a Pareto front that balances aerodynamic efficiency and formation stability. Simulation results show that the employed method generates feasible 2D and 3D formation trajectories under flight-performance constraints. The optimized formation position increases the lift-to-drag ratio from 15.8 for a single aircraft to 20.2 while maintaining favorable stability-derivative characteristics, demonstrating the benefit of introducing formation position optimization into the formation planning framework.

Keywords: UAV formation, formation trajectory planning, dynamic window approach, formation optimization

1. Introduction

With the development of electronic warfare and cooperative air combat, unmanned aerial vehicle (UAV) formations have been increasingly used in missions such as intelligence, surveillance, reconnaissance, and precision strike. Formation flight can reduce the induced drag of trailing aircraft by using the upwash generated by the wingtip vortices of leading aircraft, thereby improving fuel economy and extending flight range. Formation-flight studies have shown that an inverted-V formation can provide notable fuel savings, and that the lateral and vertical spacing between aircraft has a direct influence on the aerodynamic benefit obtained by the trailing aircraft [1, 2]. Therefore, trajectory planning for UAV formations must not only ensure obstacle avoidance and formation keeping, but also satisfy flight-performance constraints and preserve favorable relative positions during mission execution.

Various methods have been applied to UAV path planning and formation obstacle avoidance. Artificial-potential-field-based methods have been combined with genetic algorithms, virtual structures, leader-follower architectures, and consensus mechanisms to support formation keeping, obstacle avoidance, and trajectory smoothing in complex environments [3, 4, 5]. These methods are effective for describing attractive and repulsive guidance effects, but the construction of suitable potential fields

remains difficult when obstacle distributions are complex. Sampling-based and intelligent optimization methods, including RRT-based planning, ant colony optimization, and reinforcement learning, have also been used for three-dimensional route planning and dynamic obstacle avoidance [6, 7, 8]. These methods can handle multi-constraint planning problems, but their real-time performance, training cost, or direct incorporation of aircraft performance limits may restrict their application in formation flight.

The dynamic window approach (DWA) provides a real-time planning framework in which candidate velocity commands are sampled within the reachable dynamic window and evaluated through predicted trajectories. Obstacle clearance, target alignment, velocity preference, and other mission-related criteria can be included in the evaluation function, while acceleration, speed, and angular-rate limits are naturally imposed by the dynamic window itself. Improved DWA-based methods have been combined with reciprocal collision avoidance to reduce path length and flight time, and DWA-based formation planning has been used to adjust evaluation-function weights and follower positions during obstacle avoidance and formation reconfiguration [9, 10, 11]. These results indicate that DWA is suitable for formation trajectory planning where real-time decision making and flight-performance constraints must be considered simultaneously.

Three-dimensional formation planning introduces additional constraints that are not present in planar planning, including climb angle limits, altitude separation, and vertical maneuvering capability. Three-dimensional velocity obstacle methods and nonlinear-dynamic-inversion-based formation control have been used to resolve spatial conflicts and maintain formation geometry [12, 13]. Formation reconfiguration has also been formulated through convex optimization, heuristic position allocation, improved ant colony optimization, distributed predictive control, and affine transformations such as rotation, scaling, and line formation transformation [5, 14, 15, 16, 17]. These studies show that adaptive formation transformation is necessary when a formation passes through constrained airspace, but simultaneous trajectory planning for all aircraft still leads to high computational complexity.

To reduce this complexity, a leader-first trajectory planning strategy is adopted in this paper. The lead aircraft trajectory is planned by DWA, and the wingmen trajectories are generated according to the prescribed formation geometry. In the two-dimensional case, the planning process considers obstacle avoidance, target guidance, velocity preference, and flight-performance constraints. In the three-dimensional case, climb angle and velocity constraints are further introduced into the DWA evaluation process so that feasible climbing trajectories can be generated within the aircraft performance envelope. Formation contraction, rotation, line formation transformation, and recovery are used to support adaptive obstacle avoidance. For the cruise phase, a formation shape optimization model is established based on the SACCON configuration. The vortex lattice method is used to evaluate aerodynamic performance and stability-related derivatives, and NSGA-II is used to obtain a compromise solution that balances lift-to-drag improvement and formation stability.

2. Mathematical Models for Trajectory Planning and Optimization

2.1 2D Planning Method

The aircraft is modeled as a point mass. Let $\begin{bmatrix} x(t_n) & y(t_n) & \theta(t_n) & v(t_n) & \omega(t_n) \end{bmatrix}^{\mathrm{T}}$ denote the state vector at time t_n , where (x,y) represents the position in the two-dimensional plane, θ is the heading angle relative to the positive x-axis, and v denotes the flight velocity, ω is defined as the rate of change of θ. Given that the maximum linear acceleration and maximum angular acceleration are $a_{\max}$ and $\alpha_{\max}$, respectively—with the minimum acceleration being the negative of the maximum.The state update equations are

$$\begin{aligned} x(t_{n+1}) &= x(t_n) + v\cos\theta(t_n)\mathrm{d}t \\ y(t_{n+1}) &= y(t_n) + v\sin\theta(t_n)\mathrm{d}t \\ \theta(t_{n+1}) &= \theta(t_n) + \omega\mathrm{d}t \end{aligned} \tag{1}$$

where $U = \begin{bmatrix} v & \omega \end{bmatrix}^{\mathrm{T}}$ is the input value of system in 2D scenarios.

Given the time interval $\mathrm{d}t$ of the dynamic window, the set of all possible linear and angular velocities

for the lead aircraft is first computed as follows:

$$\begin{aligned} v &\in v_{limit} \cap [v(t_n) - a_{\max}\mathrm{d}t, v(t_n) + a_{\max}\mathrm{d}t] \\ \omega &\in \omega_{limit} \cap [\omega(t_n) - \alpha_{\max}\mathrm{d}t, \omega(t_n) + \alpha_{\max}\mathrm{d}t] \end{aligned} \tag{2}$$

The velocity ranges are discretized and combined pairwise to compute the reachable positions of the lead aircraft. The simulation duration corresponds to the prediction horizon, which is typically tens of times longer than the dynamic window time interval. Subsequently, the distance to the radar (obstacle) is calculated, and any trajectories that fail to ensure obstacle avoidance are discarded. An objective function is then evaluated for all remaining feasible trajectories, primarily consisting of the following components:

a. Obstacle function: defined as the distance between the leader and the obstacles;

b. Velocity function: representing the absolute magnitude of the leader's velocity;

c. Heading function: defined as the angle between the leader's flight direction and the target direction;

d. A^* function[18]: utilized to facilitate escaping from local optima. These functions are aggregated via a weighted sum;

Therefore, the 2D evaluation function can be expressed as:

$$G_{2D} = w_{obs}G_{obs} + w_v G_v + w_h G_h + w_{A^*}G_{A^*} \tag{3}$$

The trajectory yielding the maximum score is selected as the optimal trajectory for the next time step. Diverse trajectory behaviors can be obtained by adjusting these weights.
The formation configuration is represented by the formation information matrix

$$F_d = \begin{bmatrix} \rho_1 & \rho_2 & \cdots & \rho_N \\ \beta_1 & \beta_2 & \cdots & \beta_N \end{bmatrix} \tag{4}$$

where each column represents the polar coordinate position of the wingman relative to the lead aircraft.

2.2 3D Planning Method

Similarly, the aircraft is modeled as a point mass in three-dimensional space, neglecting rotational motion around the three body axes. Let $\begin{bmatrix} x(t_n) & y(t_n) & z(t_n) & v(t_n) & \theta(t_n) & \phi(t_n) & \dot{\theta}(t_n) & \dot{\phi}(t_n) \end{bmatrix}^{\mathrm{T}}$ defined as the state vector at time t_n , where (x,y,z) denotes the position of the aircraft in 3D space. θ represents the angle between the velocity vector and the positive z-axis, while ϕ represents the angle between the projection of the velocity vector on the XOY plane and the positive x-axis. The climb angle is denoted by γ, where $\gamma = \pi/2 - \theta$, and the climb angle constraint is expressed as $\gamma \leq \gamma_{\max}$. Furthermore, $\dot{\theta}$ and $\dot{\phi}$ denote the rates of change of θ and ϕ, respectively. Assuming the maximum linear acceleration and corresponding angular accelerations are known (i.e., $a_{\max}$, $\ddot{\theta}_{\max}$, and $\ddot{\phi}_{\max}$), and that the minimum acceleration is the negative of the maximum. The 3D state update equations are

$$\begin{aligned} x(t_{n+1}) &= x(t_n) + v\sin\theta(t_n)\cos\phi(t_n)\mathrm{d}t \\ y(t_{n+1}) &= y(t_n) + v\sin\theta(t_n)\sin\phi(t_n)\mathrm{d}t \\ z(t_{n+1}) &= z(t_n) + v\cos\theta(t_n)\mathrm{d}t \\ \theta(t_{n+1}) &= \theta(t_n) + \dot{\theta}\mathrm{d}t \\ \phi(t_{n+1}) &= \phi(t_n) + \dot{\phi}\mathrm{d}t \end{aligned} \tag{5}$$

where $U = \begin{bmatrix} v & \dot{\theta} & \dot{\phi} \end{bmatrix}^{\mathrm{T}}$ is the input value of system in 3D scenarios.
For the 3D planning problem, the DWA evaluation function retains the obstacle, velocity, heading, and A^* terms used in the 2D case. In addition, a climb angle evaluation term is introduced to penalize

candidate trajectories that approach or exceed the climb angle limit $\gamma_{\max}$. Therefore, the 3D evaluation function can be expressed as

$$G_{3D} = w_{\text{obs}} G_{\text{obs}} + w_v G_v + w_h G_h + w_{A^*} G_{A^*} + w_\gamma G_\gamma \tag{6}$$

where G_γ denotes the climb angle evaluation term. The candidate trajectory with the highest weighted score is selected for trajectory propagation.
In 3D scenario, the formation configuration can be represented by the formation information matrix

$$F_d = \begin{bmatrix} \rho_1 & \rho_2 & \cdots & \rho_N \\ \beta_1 & \beta_2 & \cdots & \beta_N \\ z_1 & z_2 & \cdots & z_N \end{bmatrix} \tag{7}$$

where each column represents the cylindrical coordinate position of the wingman relative to the lead aircraft.

2.3 Formation Reconstruction

Using the lead aircraft as the reference point, a local Cartesian coordinate system is established, and the position of the formation can be represented by the matrix R:

$$R = \begin{bmatrix} r_{1x} & r_{1y} \\ \cdots & \cdots \\ r_{nx} & r_{ny} \end{bmatrix} \tag{8}$$

During the flight, the formation needs to perform obstacle avoidance through maneuvers such as rotation, scaling (contraction or expansion), and line formation.
Let the rotation angle be θ_L. The rotation matrix is:

$$R(\theta_L) = \begin{bmatrix} \cos\theta_L & -\sin\theta_L \\ \sin\theta_L & \cos\theta_L \end{bmatrix} \tag{9}$$

The transformed formation position is:

$$R' = RR(\theta_L) \tag{10}$$

Let the contraction coefficient of the formation along the x-direction be κ_1, and the contraction coefficient along the y-direction be κ_2. The formation contraction matrix is:

$$R(\kappa) = \begin{bmatrix} \kappa_1 & 0 \\ 0 & \kappa_2 \end{bmatrix} \tag{11}$$

The formation contraction transformation can be expressed as:

$$R' = RR(\kappa) \tag{12}$$

Assuming the spacing distance of the line formation is d, the position matrix after the line formation transformation is:

$$R' = \begin{bmatrix} x_L & y_L \\ x_L - d\cos\psi & y_L - d\sin\psi \\ \cdots & \cdots \\ x_L - (i-1)d\cos\psi & y_L - (i-1)d\sin\psi \end{bmatrix} \tag{13}$$

where ψ is the direction angle of the line formation.

2.4 Formation Shape Optimization Method

For the cruise phase, the relative position of the wingman is optimized to balance aerodynamic efficiency and formation stability. The design vector is defined as

$$\mathbf{x} = \begin{bmatrix} \Delta x & \Delta y & \Delta z \end{bmatrix}^{\mathrm{T}}, \tag{14}$$

where Δx, Δy, and Δz are the dimensionless streamwise, lateral, and vertical spacings of the wingman relative to the lead aircraft, respectively. These variables are nondimensionalized by the wingspan of the lead aircraft and are constrained as

$$1 \le \Delta x \le 6, \quad 0 \le \Delta y \le 2, \quad -1 \le \Delta z \le 1. \tag{15}$$

For each candidate formation position, the aerodynamic coefficients are evaluated by combining AVL and OpenVSP. AVL is used for the inviscid lifting-surface calculation and provides the lift coefficient C_L and induced-drag coefficient C_{D_i} of the formation [19]. The Prandtl–Glauert compressibility correction is enabled in AVL through the freestream Mach number setting. Since the viscous zero-lift drag is not obtained from the vortex-lattice calculation in the present work, the total drag coefficient is constructed by adding the zero-lift drag coefficient computed by OpenVSP:

$$C_D(\mathbf{x}) = C_{D_i}(\mathbf{x}) + C_{D_0} \tag{16}$$

Therefore, the lift-to-drag ratio used in the optimization is calculated as

$$\frac{L}{D}(\mathbf{x}) = \frac{C_L(\mathbf{x})}{C_{D_i}(\mathbf{x}) + C_{D_0}} \tag{17}$$

The zero-lift drag coefficient is evaluated with the same reference area and flight condition as the AVL calculation. Since the aircraft geometry is fixed during the relative-position optimization, C_{D_0} is kept constant for all candidate spacings, while the induced-drag component varies with the formation position.

The stability-related objectives are based on the relative-position derivatives $\partial C_L/\partial z$, $\partial C_m/\partial z$, and $\partial C_l/\partial y$. These derivatives are obtained by perturbing the relative position and repeating the aerodynamic calculation. For a generic aerodynamic coefficient C, the central-difference approximation is

$$\frac{\partial C}{\partial \eta} \approx \frac{C(\mathbf{x} + \delta_\eta \mathbf{e}_\eta) - C(\mathbf{x} - \delta_\eta \mathbf{e}_\eta)}{2\delta_\eta}, \quad \eta \in \{y, z\} \tag{18}$$

where δ_η is the perturbation step and $\mathbf{e}_\eta$ is the unit vector in the corresponding spacing direction.

The optimization problem is solved as a multi-objective problem using the NSGA-II algorithm implemented in pygmo, the Python interface of pagmo [20]. Each individual in the population represents one candidate formation position $\mathbf{x}$. During each fitness evaluation, the formation geometry is generated, the aerodynamic coefficients are calculated, and the objective vector is assembled as

$$\min_{\mathbf{x}} \quad \mathbf{f}(\mathbf{x}) = \begin{bmatrix} -\frac{L}{D} & \frac{\partial C_L}{\partial z} & \frac{\partial C_m}{\partial z} & \frac{\partial C_l}{\partial y} \end{bmatrix}^{\mathrm{T}} \tag{19}$$

After nondominated sorting and crowding-distance selection, the Pareto front is obtained. The final formation position is selected from the Pareto front as a compromise between lift-to-drag-ratio improvement and favorable stability-derivative characteristics.

3. Results and Discussions

The trajectory planning problem considers a UAV formation composed of five aircraft, including one leader and four wingmen. All aircraft in the formation are UAVs and are assumed to have the same flight-performance limits. The formation is assigned a penetration mission from the prescribed start point to the target point while avoiding enemy threat zones. The 2D case is used to examine planar obstacle avoidance and formation contraction, whereas the 3D case further considers altitude variation, climb-angle limitation, and formation transformation. The simulation parameters used for trajectory planning are listed in Table 1. The weights of the evaluation function determine the relative importance of obstacle avoidance, velocity, target heading, global guidance, and climb angle limitation. The same parameter set is used in the following 2D and 3D simulation cases unless otherwise specified.

Table 1 – Simulation parameters used in trajectory planning

Parameter	Symbol	Value
Obstacle function weight	w_{obs}	0.02
Velocity function weight	w_v	0.12
Heading function weight	w_h	0.10
A^* function weight	w_{A^*}	0.30
Climb angle limit weight	w_γ	0.05
Time step	Δt	0.3 s
Maximum velocity	$v_{\max}$	500 m/s
Maximum heading angular rate	$\dot{\phi}_{\max}$	0.3 rad/s
Maximum polar angular rate	$\dot{\theta}_{\max}$	0.4π rad/s
Start point	P_s	(0,0,0) km
Target point	P_t	(200,200,10) km

3.1 2D Results

In the 2D case, the formation is initialized in a wedge configuration. The threat environment consists of two circular anti-aircraft threat zones. As illustrated in Figure 1, the 2D trajectory planning demonstrates that the formation automatically contracts to pass through the narrow corridor created by the air defense zones. Initially, the formation heads directly toward the target. After advancing a certain distance, the weight of the obstacle avoidance function becomes significant, prompting the entire formation to execute a left turn to evade the threat areas. As the formation approaches the target, the weight of the heading function becomes dominant, causing the formation to turn right to realign with the destination. The 2D simulation results indicate that decoupling the trajectory planning of the leader and wingmen enables the formation to successfully avoid enemy air defense zones and accomplish the penetration mission while satisfying flight performance constraints.

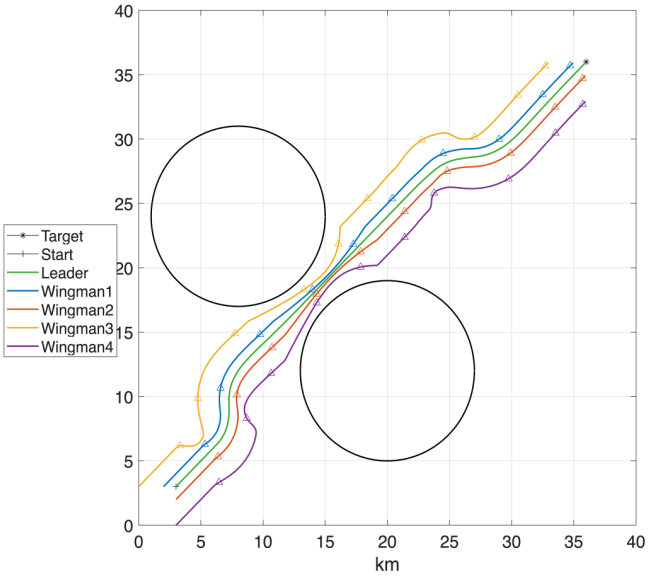


Figure 1 – Two-dimensional trajectory planning for one lead aircraft and four wingmen

3.2 3D Results

In the 3D case, the same UAV formation is initialized in an inverted-V configuration. The mission requires a climb from Point A to Point B at a higher altitude, and the threat zones are modeled as spheres. Using the two-stage decoupled planning strategy described in Section 2, the leader's three-dimensional trajectory is first generated, and the wingmen's trajectories are then derived accordingly.

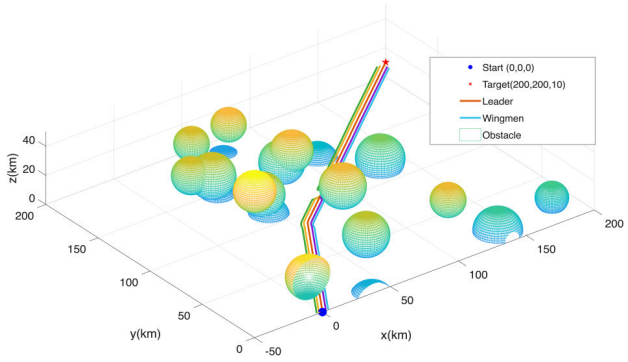


Figure 2 – Three-dimension formation flight path planning

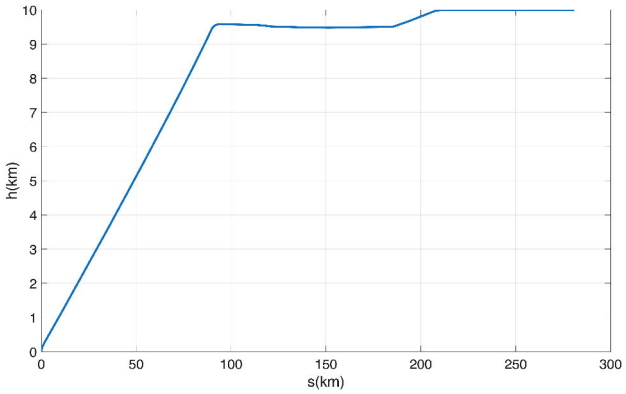


Figure 3 – Longitudinal profile of 3D formation flight path

The resulting formation trajectory is shown in Figure 2. After departure, the formation executes a turning maneuver to align with the target bearing. Following the turn, the formation first contracts laterally via the scaling matrix $R(\kappa)$, then transitions to a line formation to pass through the narrow gap between the spherical threat zones on the right. Once clear of the danger zone, the formation reverts to its initial inverted-V configuration.

The longitudinal profile is obtained by projecting the leader's trajectory onto the vertical plane, as shown in Figure 3. The profile exhibits a two-phase climbing pattern under the prescribed climb-angle limit $\gamma_{\max}$. The first climb occurs at approximately 90 km, where the formation ascends to the cruising altitude of approximately 10 km; this position coincides with the turning maneuver. The formation then maintains level flight until approximately 110 km before the target, where the second climb raises the formation to the target altitude. The two-phase pattern arises because a single continuous climb would violate the maximum climb angle given the horizontal distance available and the intervening obstacle avoidance maneuvers. This demonstrates that the DWA evaluation function automatically generates segmented climbing trajectories that satisfy the aircraft's performance envelope without explicit waypoint specification.

Figure 4 and Figure 5 further quantify the evolution of the leader's control parameters and climb velocity. During the first 700 steps, the climb angle γ converges from approximately 0.5 rad to 0.1 rad under the $\gamma_{\max}$ constraint, while the heading angle ϕ adjusts slightly from 0.8 rad to 1.0 rad, indicating minor directional corrections during the climb phase. At step 700, γ drops sharply to zero and ϕ exhibits a step decrease from 1.0 rad to 0.68 rad, corresponding to the turning maneuver upon reaching the target altitude. Concurrently, the climb velocity rises from 17 m/s to a peak of approximately 59 m/s before rapidly decaying to zero, confirming the transition to level flight. The brief velocity rise around steps 1300–1500 reflects a minor altitude adjustment for precise target arrival. These profiles are fully consistent with the two-phase climbing strategy and turning maneuver described above.

3.3 Formation Shape Optimization

During cruise, the aerodynamic benefit of formation flight depends on the relative spacing between aircraft. Therefore, the formation shape optimization method described in Section 2 is used to select a compromise wingman position. The lead aircraft and wingman adopt the same SACCON configuration [21], and the positional stability derivatives $\partial C_L/\partial z$, $\partial C_m/\partial z$, and $\partial C_l/\partial y$ are used as stability-related indicators [22, 23]. This subsection reports the resulting Pareto front, the selected design point, and the corresponding aerodynamic and stability characteristics.

The optimization results are shown in Figure 6 and Figures 7–10. The Pareto front indicates that the aerodynamic efficiency and the formation stability derivatives cannot be improved independently. A point with a smaller value of $-L/D$ corresponds to a higher lift-to-drag ratio, while smaller values of the three positional stability derivatives correspond to better formation stability in the present formulation. Therefore, the final formation geometry is selected from the Pareto front as a compromise between these two requirements, rather than as a single-objective optimum.

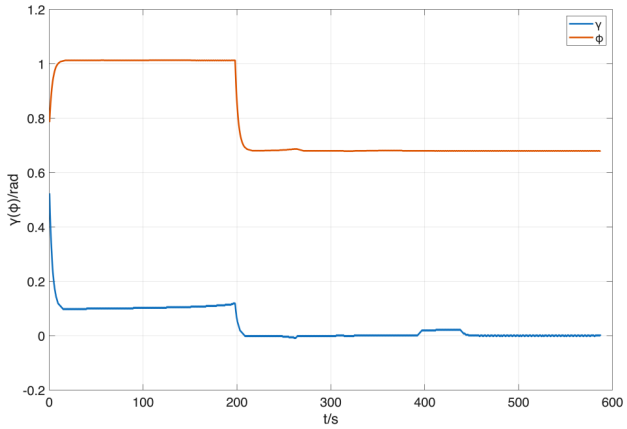


Figure 4 – Climb angle γ and heading angle ϕ of the leader

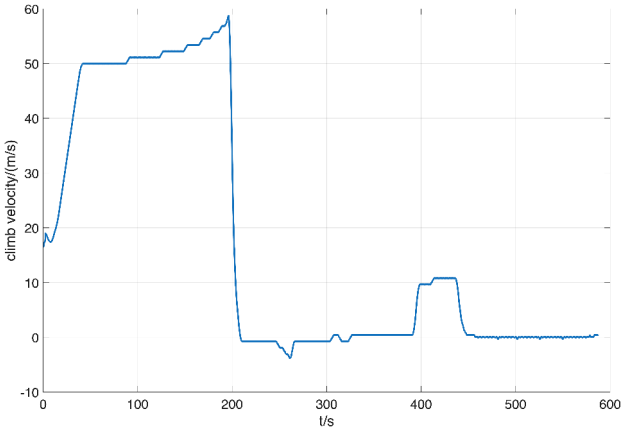


Figure 5 – Climb velocity profile of the leader

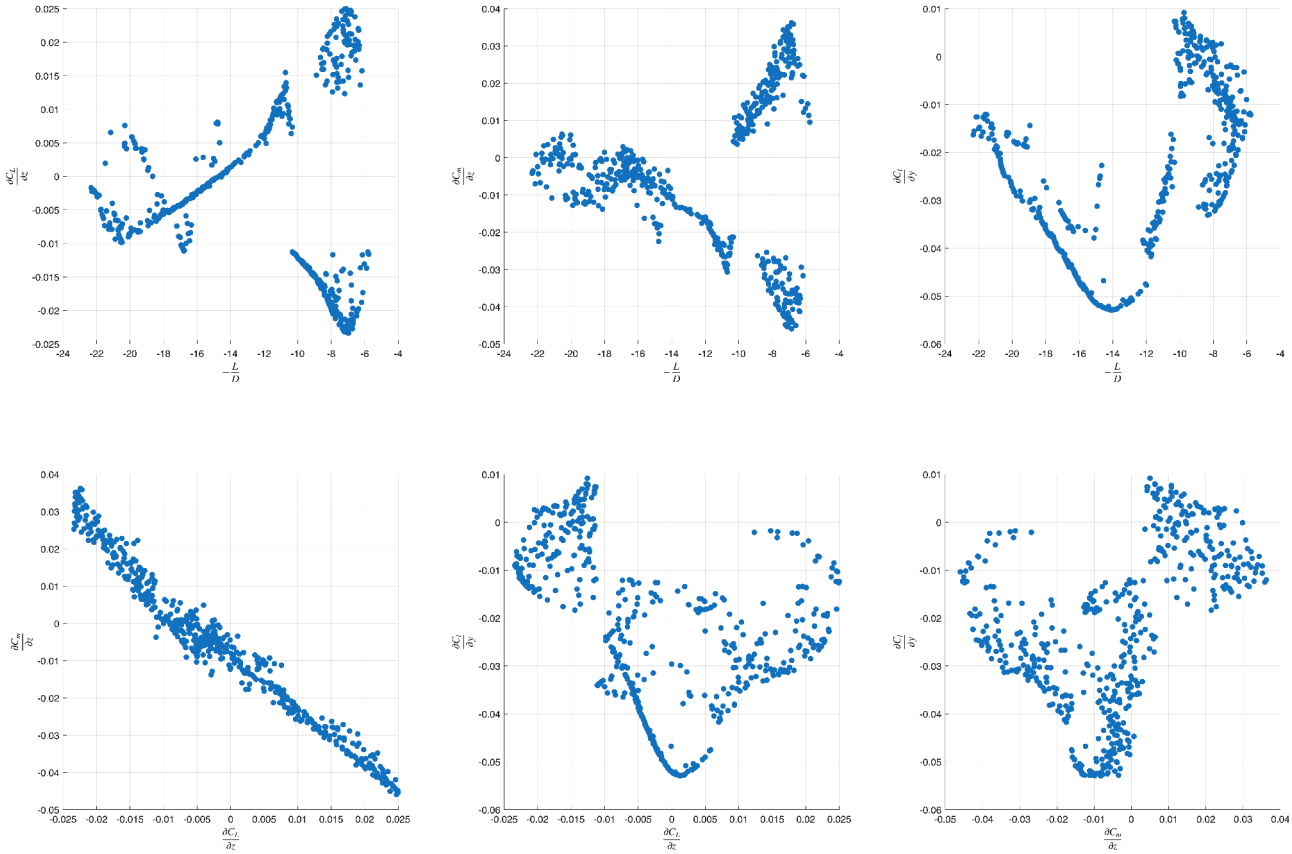


Figure 6 – Pareto front of formation optimization

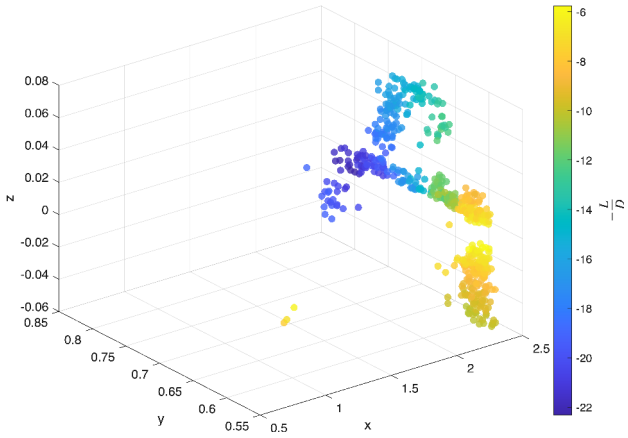


Figure 7 – Lift-to-drag ratio distribution

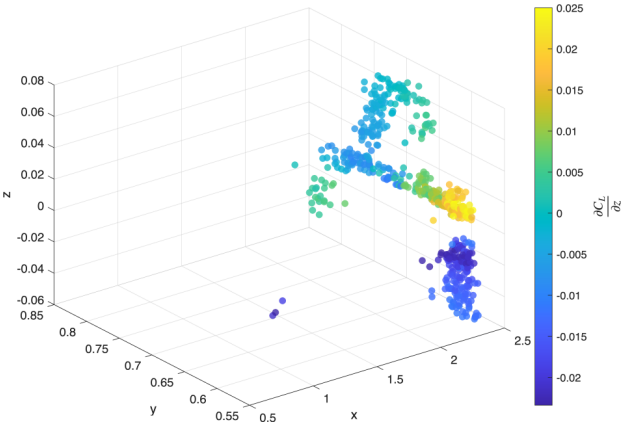


Figure 8 – Lift coefficient derivative $\partial C_L/\partial z$

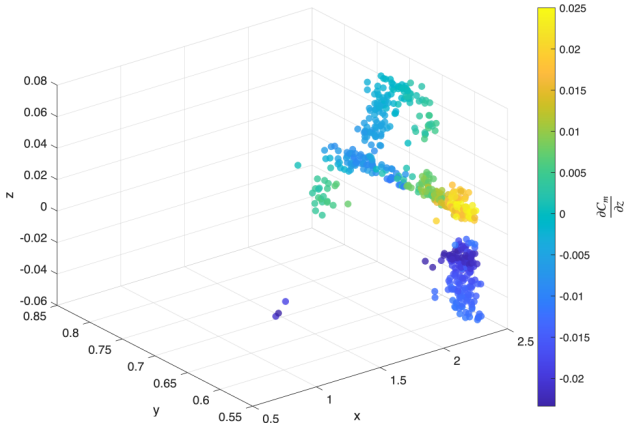


Figure 9 – Pitching moment derivative $\partial C_m/\partial z$

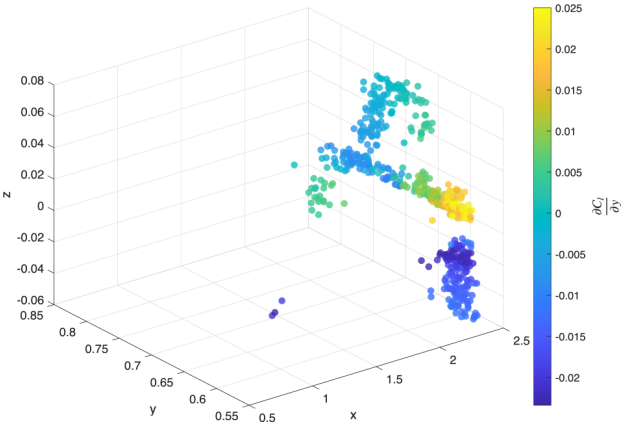


Figure 10 – Rolling moment derivative $\partial C_l/\partial y$

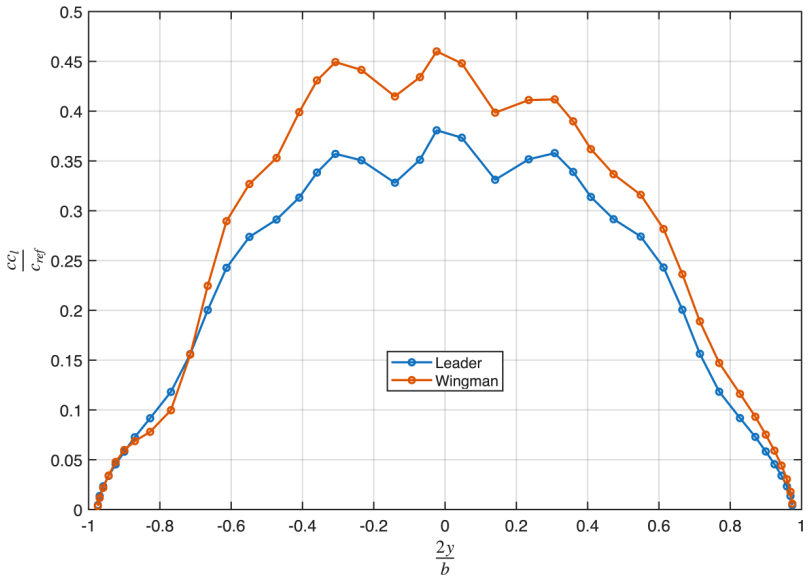


Figure 11 – Spanwise wing-loading distributions of the leader and wingman

The selected objective vector is

$$\begin{bmatrix} -L/D & \partial C_L/\partial z & \partial C_m/\partial z & \partial C_l/\partial y \end{bmatrix} = \begin{bmatrix} -20.2287 & -0.0062 & -0.0017 & -0.0252 \end{bmatrix}, \tag{20}$$

and the corresponding dimensionless design vector is

$$\begin{bmatrix} \Delta x & \Delta y & \Delta z \end{bmatrix} = \begin{bmatrix} 2.3053 & 0.7132 & 0.0100 \end{bmatrix}. \tag{21}$$

For the stability-related objectives, the selected point gives $\partial C_L/\partial z = -0.0062$, $\partial C_m/\partial z = -0.0017$, and $\partial C_l/\partial y = -0.0252$. These values show that the chosen solution does not simply pursue the largest aerodynamic benefit. Instead, it accepts a slight reduction in lift-to-drag ratio so that the stability-related derivatives, especially the pitching moment derivative, remain at more favorable values under the present optimization criterion. The individual distributions in Figures 7–10 also show that the best aerodynamic region does not exactly coincide with the most favorable stability-derivative region. The selected configuration is therefore suitable for the cruise phase, where the formation should retain aerodynamic benefit over a long duration while remaining robust to small relative-position disturbances.

Figure 11 shows the spanwise wing-loading distributions of the leader and wingman. The wingman has higher wing loading over part of the span, with the increase mainly concentrated around the midspan region. This indicates that, at the optimized relative position, the main load-bearing region of the wingman is affected by favorable aerodynamic interference. In terms of aerodynamic coefficients, the lift coefficient increases from 0.19 for the leader to 0.22 for the wingman, while the induced-drag coefficient decreases from 0.005 to 0.0039. With the same zero-lift drag coefficient, $C_{D0} = 0.00702$, the wingman lift-to-drag ratio is approximately 20.2, higher than the leader value of approximately 15.8. Therefore, the direct reason for the improvement in the wingman's lift-to-drag ratio is that the lift increases while the induced drag decreases. This improvement mainly comes from the favorable influence of the upwash induced by the leader's wingtip vortex. The upwash increases the local effective angle of attack of the wingman, increasing the wing loading in the midspan region; it also reduces the effective downwash associated with lift generation, thereby reducing induced drag.

4. Conclusions

This paper studied two-dimensional and three-dimensional trajectory planning for a UAV formation system using the dynamic window approach. A two-stage decoupled strategy was adopted, in which the leader's trajectory is planned first and the wingmen's trajectories are then generated according to the prescribed formation geometry. The main conclusions are summarized as follows:

a. The 2D simulation results show that the formation can avoid circular threat zones during a penetration mission. Through formation contraction, the aircraft pass through the narrow corridor between the threat zones and then realign with the target, indicating that the proposed method can generate feasible 2D formation trajectories under flight performance constraints.

b. In the 3D scenario, the climb angle γ is constrained in the DWA-based planning process. The formation completes turning, lateral contraction, line formation transformation, and recovery to the inverted-V configuration while avoiding spherical threat zones. The segmented climbing trajectory and the corresponding angle and velocity histories confirm that the generated path satisfies the aircraft climb performance limitation.

c. For the cruise phase, a formation shape optimization model was established by combining the SACCON configuration, the vortex lattice method, and NSGA-II. A compromise solution was selected from the Pareto front to balance aerodynamic efficiency and formation stability, increasing the lift-to-drag ratio from 15.8 for a single aircraft to 20.2 in the optimized formation.

5. Acknowledgement

6. Contact Author Email Address

author email: zhurongbo@mail.nwpu.edu.cn
corresponding author email: zhenlichen@nwpu.edu.cn

7. Copyright Statement

The authors confirm that they, and/or their company or organization, hold copyright on all of the original material included in this paper. The authors also confirm that they have obtained permission, from the copyright holder of any third party material included in this paper, to publish it as part of their paper. The authors confirm that they give permission, or have obtained permission from the copyright holder of this paper, for the publication and distribution of this paper as part of the ICAS proceedings or as individual off-prints from the proceedings.

References

[1] Geoffrey C. Bower, Tristan C. Flanzer, and Ilan M. Kroo. Formation geometries and route optimization for commercial formation flight. In *27th AIAA Applied Aerodynamics Conference*, 2009.

[2] Jia Cheng Chan, Henrik Hesse, and Peng Cheng Wang. Aerodynamic interactions in formation flight for wake vortex surfing. In *AIAA AVIATION 2023 Forum*, 2023.

[3] Hao Chen, Juntong Qi, Mingming Wang, Chong Wu, Yansheng Liu, and Yuan Ping. A hybrid GA-APF 3d trajectory planning method for large-scale UAV formation systems. In *2023 42nd Chinese Control Conference (CCC)*, pages 6024–6030, 2023.

[4] A. Mirzaee Kahagh, F. Pazooki, S. Etemadi Haghighi, and D. Asadi. Real-time formation control and obstacle avoidance algorithm for fixed-wing UAVs. *The Aeronautical Journal*, 126(1306):2111–2133, 2022.

[5] Yilin Zhong. Research on formation keeping and obstacle avoidance methods for UAVs. Master's thesis, Dalian Jiaotong University, 2025.

[6] Kaiwen Zheng, Chengze Du, Xingfang Zhao, and Xiaofan Pang. Integrating spatio-temporal hash in three-dimensional RRT* multi-formation route planning. *Systems Engineering and Electronics*, 47(7):2256–2266, 2025.

[7] Yongchao Zhang, Xiaoguang Gao, Zihao Guo, Dawei Guo, and Yiyang Jiang. Improved ant colony optimization for multi-UAV three-dimensional trajectory planning in SEAD missions. *International Journal of Transportation Science and Technology*, 17:254–268, 2025.

[8] Jiaxin Li, Junyan Hu, Jiaming Che, and Dongbing Gu. Real-time autonomous obstacle avoidance method for UAV in a three-dimensional dynamic environment. *The Aeronautical Journal*, 129(1331):195–218, 2025.

[9] Dieter Fox, Wolfram Burgard, and Sebastian Thrun. The dynamic window approach to collision avoidance. *IEEE robotics & automation magazine*, 4(1):23–33, 2002.

[10] Yuxin Chang and Xingsheng Gu. Improved dynamic window approach fused with optimal reciprocal collision avoidance for multi-uav autonomous obstacle avoidance. *Scientific Reports*, 15:4752, 2025.

[11] Lingxia Mu, Zhengjun Zhou, Ban Wang, Youmin Zhang, Xianghong Xue, and Kaikai Ning. Formation obstacle-avoidance and reconfiguration method for multiple UAVs. *Journal of Computer Applications*, 44(9):2938–2946, 2024.

[12] Yazdi I. Jenie, Erik-Jan van Kampen, Coen C. de Visser, Joost Ellerbroek, and Jacco M. Hoekstra. Three-dimensional velocity obstacle method for uncoordinated avoidance maneuvers of unmanned aerial vehicles. In *AIAA Guidance, Navigation, and Control Conference*, 2015.

[13] Erfu Yang, Yoichiro Masuko, and Tsutomu Mita. Dual-controller approach to three-dimensional autonomous formation control. *Journal of Guidance, Control, and Dynamics*, 27(3):470–478, 2004.

[14] Behçet Açıkmeşe, Daniel P. Scharf, Emmanuell A. Murray, and Fred Y. Hadaegh. A convex guidance algorithm for formation reconfiguration. In *AIAA Guidance, Navigation, and Control Conference and Exhibit*. Jet Propulsion Laboratory, California Institute of Technology, 2005.

[15] Yu Wu, Shuting Xu, Wei Dai, and Liyang Lin. Heuristic position allocation methods for forming multiple UAV formations. *Engineering Applications of Artificial Intelligence*, 118:105654, 2023.

[16] Yingying Cai, Wei Wang, Changcheng Wang, and Peng Fan. Research on formation transformation algorithm of UAV formation. *Journal of Ordnance Equipment Engineering*, 46(7):249–255, 2025.

[17] Changjian Ru, Ruixuan Wei, Jing Dai, Dong Shen, and Lipeng Zhang. Autonomous reconfiguration control method for UAV's formation based on Nash bargain. *Acta Automatica Sinica*, 39(8):1349–1359, 2013.

[18] Dario Calogero Guastella, Nunzio Dario Cavallaro, Carmelo Donato Melita, Maurizio Savasta, and Giovanni Muscato. 3d path planning for uav swarm missions. In *Proceedings of the 2018 2nd International Conference on Mechatronics Systems and Control Engineering*, pages 33–37, 2018.

[19] Mark Drela and Harold Youngren. *AVL 3.36 User Primer*. Massachusetts Institute of Technology, 2017.

[20] Francesco Biscani and Dario Izzo. A parallel global multiobjective framework for optimization: pagmo. *Journal of Open Source Software*, 5(53):2338, 2020.

[21] Andreas Schütte, Dietrich Hummel, and Stephan Hitzel. Numerical and experimental analyses of the vortical flow around the saccon configuration. In *28th AIAA Applied Aerodynamics Conference*, 2010.

[22] A. W. Bloy, M. G. West, K. A. Lea, and M. Joiima'a. Lateral aerodynamic interference between tanker and receiver in air-to-air refueling. *Journal of Aircraft*, 30(5):705–710, 1993.

[23] William B. Blake and David R. Gingras. Comparison of predicted and measured formation flight interference effects. *Journal of Aircraft*, 41(2):201–207, 2004.